J. Fluid Mech. (2008), *vol.* 599, *pp.* 29–50.
doi:10.1017/S0022112007009342 Printed in the United Kingdom

Two-dimensional instabilities of time-dependent zonal flows: linear shear

ANDREI NATAROV, KELVIN J. RICHARDS AND JULIAN P. McCREARY JR

International Pacific Research Center, University of Hawaii, Honolulu, Hawaii, USA

(Received 25 August 2006 and in revised form 25 September 2007)

In this study, we investigate the stability of time-dependent zonal flows to two-dimensional (zonally symmetric) disturbances. While steady currents can only experience *inertial instability* (II) in this setting, unsteady ones may be destabilized in other ways. For example, time-periodic flows can be subject to *parametric subharmonic instability* (PSI). Motivated by observations of salinity interleaving patterns in the upper equatorial Pacific Ocean, our objective is to determine the basic properties of dominant instabilities (their generation mechanism, spatial and temporal characteristics, and finite-amplitude development) for background flows that are representative of those in the upper-equatorial ocean, yet still amenable to a computational sweep of parameter space. Our approach is to explore the stability of solutions to linear and nonlinear versions of a two-dimensional model for an idealized background flow with oscillating linear shear. To illustrate basic properties of the instabilities, the f-plane and equatorial β-plane scenarios are studied using a linear model. Stability regime diagrams show that on the f-plane there is a clear separation in dominant vertical scales between PSI- and II-dominated regimes, whereas on the equatorial β-plane the parameter space contains a region where dominant instability is a mixture of the two types. In general, PSI favours lower vertical modes than II. The finite-amplitude development of instabilities on the equatorial β-plane is explored using a nonlinear model, including cases illustrating the equilibration of pure II and the development of pure PSI and mixed instabilities. We find that unless the instabilities are weak enough to be equilibrated by viscosity at low amplitude, disturbances continue to grow until the vertical shear of their meridional velocity field becomes large enough to allow for Richardson numbers less than $1/4$; as a consequence, PSI-favoured vertical modes are able to reach higher amplitudes than II-favoured modes before becoming susceptible to Kelvin–Helmholtz instability, and induce tracer intrusions of a considerably larger meridional extent.

1. Introduction

In this paper, we study the stability of time-dependent zonal currents with respect to two-dimensional (zonally symmetric) disturbances. Instabilities arising in this situation include inertial instability (II), which requires violation of the condition $fQ \geqslant 0$ somewhere in the flow domain, where f is the Coriolis parameter and Q is the potential vorticity of the background flow, as well as instabilities that occur only in time-dependent flows. A familiar instability of the latter sort is parametric subharmonic instability (PSI), which occurs for periodic time dependence. Flow regimes conducive to these instabilities are prevalent near the equator, particularly in

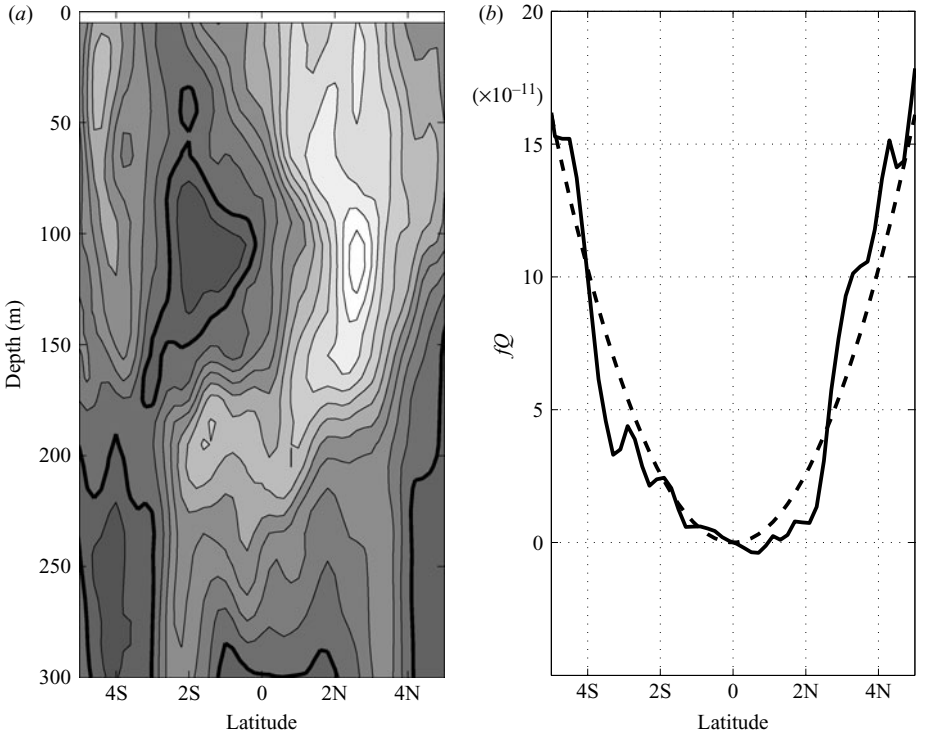

FIGURE 1. (*a*) A snapshot of zonal velocity profile observed at 165°E in July 2001. Contour interval is $0.1\,\mathrm{m\,s^{-1}}$. Light shades indicate eastward flow. The thick black line corresponds to the zero contour. (*b*) The corresponding fQ (solid line) contrasted with f^2 (dashed line). The background potential vorticity Q is defined as $f - U_y$, where U is the zonal component of velocity averaged between 100 and 150 m. A steady zonal flow is susceptible to inertial instability if the solid line drops below zero somewhere in the domain. (Data source: G. Johnson, PMEL.)

the upper ocean, and the focus of this study is on understanding the properties of unstable disturbances there. (Throughout the text, we refer to a region that satisfies the aforementioned inequality as a region of 'anomalous Q.')

The upper equatorial ocean has a system of vigorous zonal jets with meridional and vertical shears, and is influenced by free, equatorially trapped waves (Philander 1990). Snapshots of the flow field in the western Pacific often show transient zonal jets swifter than $1\,\mathrm{m\,s^{-1}}$, with a width scale of only 50 km and displaced off the equator by more than 1°, which contain regions of anomalous Q (figure 1*a*).

In addition, interleaving structures are often visible in the salinity field of the thermocline in the equatorial Pacific, taking the form of small vertical scale ($\sim$10 m) intrusions that can extend meridionally a few hundred kilometres and zonally in excess of 1000 km (Richards & Banks 2002; Lee & Richards 2004). They probably result from dynamical processes in the equatorial ocean, and indeed they have a spatial structure consistent with that of II cells. Time-mean profiles of the flow in the upper equatorial ocean, however, are usually only weakly inertially unstable, and equilibration studies suggest that they are incapable of producing interleaving (Richards & Edwards 2003). On the other hand, individual meridional sections of the zonal component of the flow exhibit broad regions of anomalous Q, and so are susceptible to inertial instability if the flow is assumed steady (figure 1*b*). In such

cases, the instability will produce interleaving structures similar to those observed (Edwards & Richards 1999; Richards & Edwards 2003).

Linear stability of steady equatorial currents to zonally symmetric perturbations was originally addressed in the studies of Dunkerton (1981) and Stevens (1983). The only possible instability in this case is II. Unstable modes form cells in the meridional-vertical plane, with a small vertical scale determined by vertical mixing and a large meridional scale determined by either domain boundaries, the Rossby radius of deformation of the unstable vertical mode, or the meridional extent of the unstable region. Since vertical mixing is an uncertain quantity in geophysical applications, the question of vertical scale selection in realistic flows remains unresolved by these studies. In the limit of small vertical mixing, linear theory predicts that disturbances with the smallest vertical scale will eventually dominate the flow, suggesting that nonlinear processes are likely to play an important role in scale selection.

The nonlinear development and equilibration of steady background flows has been studied by Hua, Moore & Le Gentil (1997) and Griffiths (2003*a*, *b*). The nonlinear process that has received most attention in these studies is the neutralization of the anomalous Q region. A nonlinear vertical scale selection mechanism for the case of strong inertial instability has been suggested by Griffiths (2003*b*). The main idea is that the highest vertical modes with the fastest linear growth rates become unstable to Kelvin–Helmholtz instability and dissipate before they completely neutralize the anomalous Q region. The equilibrated state is therefore dominated by a disturbance with a finite vertical scale.

d'Orgeville & Hua (2005) examined time-periodic flows, with application to subthermocline currents in the equatorial ocean. They have shown that a vertical mode-1 standing, zonally independent, mixed Rossby–gravity (Yanai) wave undergoes PSI on a time scale of a few thousand days, leading to formation of structures with vertical scales 7–8 times smaller than that of the background wave. The dominant vertical scale in their study is determined by resonant properties of PSI, rather than by the value of the vertical mixing coefficient. Similar to II, the nonlinear development leads to mixing of vertically averaged potential vorticity in the vicinity of the equator.

The impact of the time dependence of the background flow on the stability and equilibration of the system must be determined. Here we explore the existence of both II and time-dependent instabilities. For this purpose, we obtain solutions to both the linear and nonlinear versions of a two-dimensional (zonally independent) model, considering the stability of flows with time-dependent linear meridional shear $U(y, t) = \Lambda(t)y$. The linear solutions illustrate the dependence of the instabilities on model parameters and on the background current, whereas the nonlinear solutions determine their post-linear development and equilibration. The assumption of linear shear allows a thorough analysis of the problem and provides insight into the stability of more realistic flow profiles to be considered in a follow-up study.

In this study, we extend previous work by providing a unifying framework for II and PSI. We explore the effect of flows with oscillatory and mean shear, determining the generation mechanism (II, PSI, or both), growth rates, vertical scales and meridional structure of the resulting unstable modes for a wide range of parameter values. We also address the nonlinear development of instabilities in different parts of the parameter space – where II is the dominant instability, where the only instability is pure PSI, and where the dominant linear instability is of a mixed type.

The paper is organized as follows. Section 2 describes the ocean model. Section 3 introduces the concepts of II and time-dependent instabilities, considering background zonal flows with steady and time-varying linear shear on an f-plane (§ 3.1), which

most easily illustrate basic properties of the instabilities, and on an equatorial β-plane (§ 3.2). Parameter ranges in which either II or time-dependent instabilities dominate, and in which they interact, are determined. Section 4 discusses the nonlinear evolution of the instabilities on the equatorial β-plane. Section 5 provides a summary and discussion of results.

2. The model

The model describes the temporal development of a two-dimensional zonally symmetric (x-independent) flow field. The vanishing of the zonal derivative in the continuity equation allows a streamfunction, ψ, defined by

$$v = -\psi_z, \qquad w = \psi_y, \tag{2.1}$$

to be introduced, where v and w are the meridional (northward) and vertical (upward) components of velocity, respectively. The governing equations for zonal velocity u, zonal vorticity $\nabla^2\psi$, and density ρ can then be written

$$u_t + f\psi_z = -J(\psi, u) + \nu_h u_{yy} + \nu_v u_{zz} + F(y, t), \tag{2.2a}$$

$$\nabla^2\psi_t - f u_z + \frac{g}{\rho_*}\rho_y = -J(\psi, \nabla^2\psi) + \nu_h\nabla^2\psi_{yy} + \nu_v\nabla^2\psi_{zz}, \tag{2.2b}$$

$$\rho_t = -J(\psi, \rho) + \kappa_h\rho_{yy} + \kappa_v\rho_{zz}. \tag{2.2c}$$

where $J(\xi, \eta) = \xi_y\eta_z - \xi_z\eta_y$ is the Jacobian operator, ρ_* is the reference density, $\nu_{h,v}$ are horizontal and vertical viscosities, $\kappa_{h,v}$ are horizontal and vertical diffusivities, respectively, and $F(y, t)$ is a vertically uniform forcing.

It is convenient to separate the flow into background and perturbation parts $u = U(y, t) + u'$, $\rho = \rho_b(z) + \rho'$, where the background zonal velocity satisfies $U_t = F(y, t)$. Here, we restrict the background zonal velocity to the form

$$U(y, t) = \Lambda(t)y,$$

which is equivalent to setting $F(y, t) = [\mathrm{d}\Lambda(t)/\mathrm{d}t]\, y$ in (2.2a), and the background density to

$$\rho_b(z) = \rho_* \left(1 - \frac{N^2}{g}z\right),$$

where N is the background buoyancy frequency, here assumed constant, and g is the acceleration due to gravity.

The perturbation fields are then governed by

$$u_t + [f - \Lambda(t)]\psi_z = -J(\psi, u) + \nu_h u_{yy} + \nu_v u_{zz}, \tag{2.3a}$$

$$\nabla^2\psi_t - f u_z + \frac{g}{\rho_*}\rho_y = -J(\psi, \nabla^2\psi) + \nu_h\nabla^2\psi_{yy} + \nu_v\nabla^2\psi_{zz}, \tag{2.3b}$$

$$\rho_t - \frac{\rho_* N^2}{g}\psi_y = -J(\psi, \rho) + \kappa_h\rho_{yy} + \kappa_v\rho_{zz}, \tag{2.3c}$$

where primes on u, ψ and ρ have been dropped.

Solutions to (2.3) (the nonlinear model) are found in a channel $0 \leqslant z \leqslant H$ and $-L \leqslant y \leqslant L$. Periodic boundary conditions are applied in z and no normal flow and free-slip conditions are imposed on the sidewalls at $\pm L$. Solutions are obtained by introducing a perturbation and integrating an initial-value problem using the

numerical code of Hua *et al.* (1997). Parameters, initial conditions, and grid resolution are given in § 4. When unstable stratification arises somewhere in the flow domain, the diffusivity coefficient is temporarily increased by a factor of 10 in that part of the domain.

We simplify (2.3) further by dropping the nonlinear terms $J(\psi, \cdot)$, assuming that $\nu_v = \kappa_v = \nu$ and $\nu_h = \kappa_h = 0$, and adopting the hydrostatic approximation (the linear model). In that case, solutions to (2.3) can be represented as $q = q_m(y, t)\exp(\mathrm{i}mz) + c.c.$ where q is u, ψ, or ρ, allowing the replacement of ∂_z with $\mathrm{i}m$. Writing the simplified version of (2.3) as a single equation in v_m ($= -\mathrm{i}m\psi_m$) yields

$$\left[\mathscr{D}_m^2 - c_m^2\partial_{yy} + fQ(t)\right]v_m = 0, \tag{2.4}$$

where $\mathscr{D}_m = \partial_t + \nu m^2$, $c_m^2 = N^2/m^2$, and $Q(t) = f - \Lambda(t)$ is the background potential vorticity. Since meridional viscosity and diffusivity coefficients are set to zero in the linear model, solutions to (2.4) are only required to satisfy the no-normal-flow boundary conditions $v_m = 0$ at $y = \pm L$.

3. Linear solutions

In this section, we obtain solutions to (2.4) on the f-plane (§ 3.1) and equatorial β-plane (§ 3.2). The f-plane set-up allows a simple analytic treatment, which elucidates the subject, whereas the equatorial β-plane case corresponds to a more geophysically relevant situation.

3.1. *f-plane solutions*

When f is constant, solutions to (2.4) can be found in the form

$$v_m(y, t) = \sum_{j=1}^{\infty} v_{mj}(t)\sin\ell_j(y + L), \tag{3.1}$$

where $\ell_j = \pi j/(2L)$ to ensure that there is no normal flow through the channel walls. It follows that each v_{mj} satisfies

$$\left[\mathscr{D}_m^2 + \sigma_{mj}^2(t)\right]v_{mj} = 0, \tag{3.2}$$

with

$$\sigma_{mj}^2(t) = fQ(t) + \ell_j^2 c_m^2. \tag{3.3}$$

Without loss of generality, we assume that $f > 0$, and for notational convenience we drop subscripts m and j in the rest of this subsection.

3.1.1. *Inertial instability*

To review relevant properties of II, we set $\Lambda(t)$ to a constant value $\bar{\Lambda}$ to eliminate any influence of time-dependent instability. Since $\sigma^2 = f(f - \bar{\Lambda}) + \ell^2 c^2$ is then constant, solutions have the form

$$v(t) = a\exp(s^+ t) + b\exp(s^- t), \tag{3.4}$$

where

$$s^{\pm} = \pm|\sigma|\exp\left\{\mathrm{i}\frac{\pi}{4}[1 + \mathrm{sgn}(\sigma^2)]\right\} - \nu m^2 \tag{3.5}$$

and $\mathrm{sgn}(\cdot)$ is the sign function.

According to (3.3) and (3.5), it follows that a growing instability exists when

$$\bar{\Lambda} > f + \frac{\ell^2 c^2 + \nu^2 m^4}{f}, \tag{3.6}$$

so that s^+ is real and positive. In this case, a and b are the initial amplitudes of growing and decaying modes, respectively.

For fixed f, N and $\bar{\Lambda}$, the inviscid growth rate

$$s^+ = \sqrt{f(\bar{\Lambda} - f) - N^2\alpha^2} \tag{3.7}$$

is uniquely determined by the ratio $\alpha = \ell/m$, and reaches a maximum at $\alpha = 0$. Thus, in the case of a horizontally unbounded ocean ($L \to \infty$), all vertical modes have the same growth rate, independent of m, and there is no mechanism for vertical-scale selection.

The smallest vertical scale ($|m| \to \infty$) is selected as dominant only if L is set to a finite value. In this case, if the initial disturbance is not band-limited in m, the dominant vertical scale will monotonically decrease with time (except for the special case when vertical wavenumbers larger than some finite value all project onto decaying modes). When viscosity is added to the governing equations, the 'cascade' to higher vertical wavenumbers is halted at the wavenumber that first reverses the inequality (3.6). Note that for a given m, the fastest-growing mode also favours the smallest ℓ ($j = 1$). Thus, assuming that the initial disturbance also is not band-limited meridionally, there will also be a 'cascade' towards larger meridional scales.

3.1.2. *Time-dependent instability*

Studies on time-dependent instability usually focus on the case of time-periodic background flow, for example

$$\Lambda(t) = \bar{\Lambda} - \delta\Lambda \cos\frac{2\pi t}{T}, \tag{3.8}$$

where $\delta\Lambda$ is the amplitude of the oscillatory shear. On the f-plane we obtain the Mathieu equation, which has been extensively studied (e.g. Stoker 1950).

Solutions to the Mathieu equation can be found analytically or numerically to any degree of accuracy. However, it is difficult to build physical intuition about time-dependent instabilities, except in the case of small $\delta\Lambda$, where physically interpretable solutions can be found by the method of multiple scales (Bender & Orszag 1978). This analysis reveals that the flow becomes unstable to perturbations whose natural frequency $\bar{s}$ in a time-mean shear $\bar{\Lambda}$ satisfies $\bar{s} = p\pi/T$, where p is an integer, with the resonance corresponding to $p = 1$ having the fastest growth rate (later in this section, we refer to it as the 'dominant resonance' – see (3.23)). The method of multiple scales can also be used to extend the analysis to finite $\delta\Lambda$, but calculations become increasingly cumbersome and less illuminating. Information about the physics of the phenomenon is hard to extract from higher-order corrections to the multiple-scales solution, while the physical interpretation of the instability mechanism must be modified, as the meaning of the term 'natural frequency' of the perturbation is unclear when the magnitude of oscillatory shear becomes large.

To make progress in understanding the mechanism of instability without being restricted to small oscillatory shears we assume that $\Lambda(t)$ is a square wave with

period T,

$$\Lambda(t) = \bar{\Lambda} - \delta\Lambda \operatorname{sgn}\left(\cos\frac{2\pi t}{T}\right), \tag{3.9}$$

in which case the background shear switches between $\bar{\Lambda} \mp \delta\Lambda$ at times $t_n = -T/4 + nT/2$. With this choice for $\Lambda(t)$, the f-plane solutions can be found analytically, allowing basic properties of II and time-dependent instabilities to be clearly identified and interpreted in terms of a more physically transparent steady background state dynamics. At the same time, solutions for square-wave $\Lambda(t)$ are very similar to solutions for cosine-wave $\Lambda(t)$ given by (3.8), as we show later in this section.

To separate dynamical from dissipative decay of modes, we set $\nu = 0$ in this section. With this restriction, (3.2) becomes

$$v_{tt} + \sigma_k^2 v = 0, \tag{3.10}$$

where

$$\sigma_k^2 = f(f - \Lambda_k) + N^2\alpha^2, \tag{3.11}$$

$k = 0$ for $t_{2n} < t \leqslant t_{2n+1}$, and $k = 1$ otherwise, and $\Lambda_{\binom{0}{1}} = \bar{\Lambda} \mp \delta\Lambda$.

Solutions to (3.10) can be obtained that are similar over time intervals $t_{2n} < t \leqslant t_{2n+2}$, differing only in their amplitude. To describe the complete solution, then, it is sufficient to obtain the solution only in the interval $t_0 < t \leqslant t_0 + T = t_2$ and to find the amplification factor for the subsequent interval. For our purpose, it is convenient to write the general solution to (3.10) in the form

$$v = \begin{cases} A\cos[\omega_0(t - t_0) + \theta_0], & t_0 < t \leqslant t_1, \\ B\cos[\omega_1(t - t_1) + \theta_1], & t_1 < t \leqslant t_2, \\ C\cos[\omega_0(t - t_2) + \theta_2], & t_2 < t \leqslant t_3, \end{cases} \tag{3.12}$$

where

$$\omega_k = \mathrm{i}\,|\sigma_k| \exp\left\{\mathrm{i}\frac{\pi}{4}\left[1 + \operatorname{sgn}\left(\sigma_k^2\right)\right]\right\} \tag{3.13}$$

and θ_0 and θ_1 are phases to be determined. Requiring continuity of the perturbation fields u, v and ρ in time, it follows that the appropriate matching conditions are continuity of v and v_t at t_1 and t_2.

For the jump at t_1, the matching conditions give

$$\begin{aligned} A\cos(\omega_0 T/2 + \theta_0) &= B\cos\theta_1, \\ \omega_0 A\sin(\omega_0 T/2 + \theta_0) &= \omega_1 B\sin\theta_1, \end{aligned} \tag{3.14}$$

which yield

$$\frac{B^2}{A^2} = 1 + \left(\frac{\omega_0^2}{\omega_1^2} - 1\right)\sin^2(\omega_0 T/2 + \theta_0). \tag{3.15}$$

Although the derivations presented in this subsection are valid for all values of Λ_k, for the purposes of the discussion we now assume further that Λ_k are both below critical value, eliminating the possibility of II. Both ω_0 and ω_1 are real in this case, and hence any instability we find is pure PSI in nature. Since $\Lambda_0 < \Lambda_1$ it follows from the dispersion relation that $\omega_0^2/\omega_1^2 > 1$ and the ratio B^2/A^2 can be no smaller than one. The amplification factor, however, depends on the phase of the disturbance at the time of the jump. Matching the solutions across the jump at t_2 results in

$$\frac{C^2}{B^2} = 1 + \left(\frac{\omega_1^2}{\omega_0^2} - 1\right)\sin^2[\omega_1 T/2 + \theta_1], \tag{3.16}$$

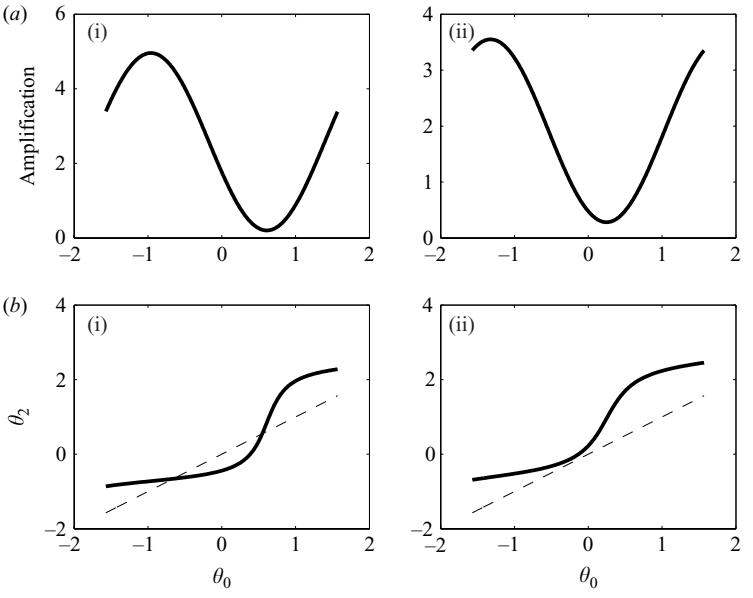

FIGURE 2. (*a*) Amplification factor C^2/A^2 and (*b*) phase map $\theta_{n+2}(\theta_n)$ (solid curves) for (i) unstable and (ii) stable modes. Curves are plotted in the range $-\pi/2 \leqslant \theta_0 \leqslant \pi/2$, and intersections between the solid and dashed ($\theta_2 = \theta_0$) curves are values of θ_0 for fixed-point solutions to (3.10).

which is no larger than 1 since $\omega_1^2/\omega_0^2 < 1$. The question of stability is therefore about whether the decrease is greater or less than the increase during the first half of the cycle. The overall amplification factor through a single period is then given by

$$\frac{C^2}{A^2} = \left\{1 + \left(\frac{\omega_0^2}{\omega_1^2} - 1\right) \sin^2(\omega_0 T/2 + \theta_0)\right\} \left\{1 + \left(\frac{\omega_1^2}{\omega_0^2} - 1\right) \sin^2(\omega_1 T/2 + \theta_1)\right\}. \tag{3.17}$$

The phase θ_2 at the beginning of the new cycle (at time t_2) is given by

$$\theta_2 = \tan^{-1}\left[\frac{\omega_0}{\omega_1} \tan(\omega_1 T/2 + \theta_1)\right], \tag{3.18}$$

where

$$\theta_1 = \tan^{-1}\left[\frac{\omega_1}{\omega_0} \tan(\omega_0 T/2 + \theta_0)\right]. \tag{3.19}$$

Since we seek solutions that are similar for each cycle, we require that $\theta_2(\theta_0) = \theta_0$ (a fixed-point solution) and solve for θ_0. The solution is given by

$$\tan\theta_0 = \frac{\tau_0\tau_1(\mathscr{W}^2 - 1)}{2\mathscr{W}(\tau_0 + \mathscr{W}\tau_1)} \pm \frac{\sqrt{\tau_0^2\tau_1^2(\mathscr{W}^2 - 1)^2 - 4\mathscr{W}(\tau_0 + \mathscr{W}\tau_1)(\tau_1 + \mathscr{W}\tau_0)}}{2\mathscr{W}(\tau_0 + \mathscr{W}\tau_1)}, \tag{3.20}$$

where $\mathscr{W} = \omega_0/\omega_1$ and $\tau_k = \tan\omega_k T/2$.

Figure 2 shows two qualitatively different examples of phase maps (figure 2*b*) and corresponding amplification factors (figure 2*a*). Figures 2(*a*)(i) and 2(*b*)(i) show the case when the phase map has a stable fixed point. In this case, the state vector converges toward the fixed point that corresponds to an amplification factor larger than one. The growth rate for the disturbance is obtained by substitution of the

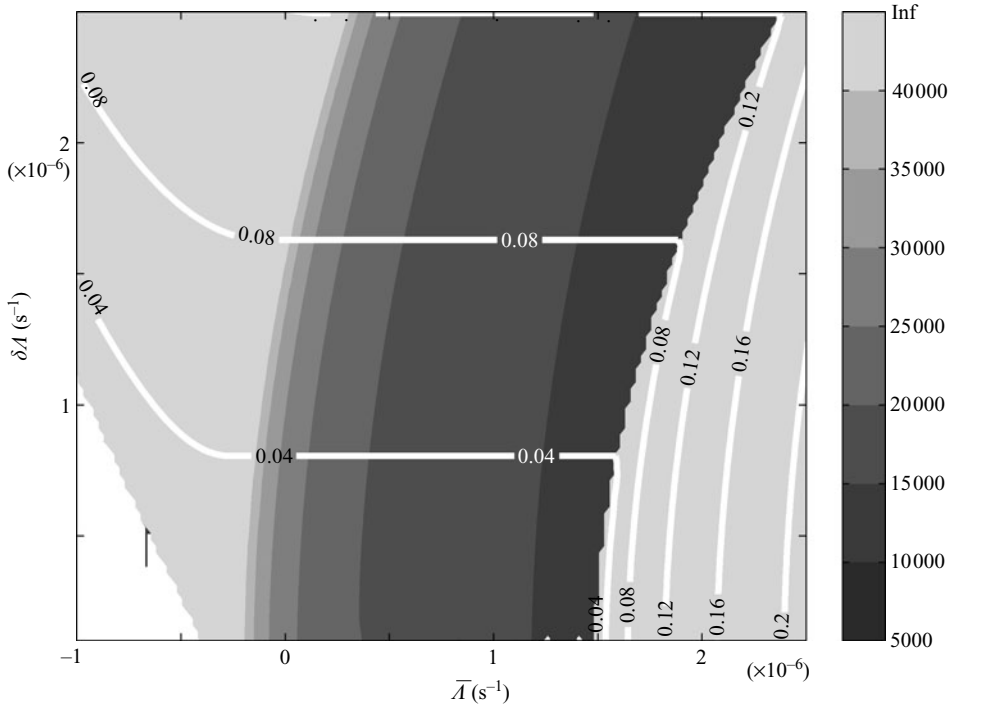

FIGURE 3. A stability-regime diagram in $(\bar{\Lambda}, \delta\Lambda)$-space and on the f-plane, plotting slope α^{-1} (shading) and growth rate γ in days^{-1} (contours) for the fastest-growing inviscid unstable mode when the environmental parameters have the values given in the text.

root (3.20) that corresponds to the growing mode into the equation for C^2/A^2. Figures 2(*a*)(ii) and 2(*b*)(ii) show the case when fixed points do not exist. The state vector in this case never becomes phase-locked, and throughout its evolution has amplification factors both below and above 1. Transient growth is possible in this case for a finite time interval. The Floquet theorem (Bender & Orszag 1978) implies that no indefinitely sustained exponential growth will occur.

Instability is therefore connected to the existence of fixed points of the map $\theta_2(\theta_0)$. When a fixed point θ_0 exists, such that $C^2/A^2(\theta_0) > 1$, the amplification factor can alternatively be written as

$$\frac{C^2}{A^2} = \frac{1 + \left(\mathscr{W}^2 - 1\right)\sin^2\left(\omega_0 T/2 + \theta_0\right)}{1 + \left(\mathscr{W}^2 - 1\right)\sin^2\left(\theta_0\right)}. \tag{3.21}$$

The growth rate γ is defined by

$$\gamma = \frac{1}{2T}\log\left(\frac{C^2}{A^2}\right), \tag{3.22}$$

an analytic expression that is a function of f, N, T, $\bar{\Lambda}$, $\delta\Lambda$ and α. The viscous growth rate is easily obtained by subtracting νm^2 from γ. For the plots discussed next, the environmental parameters (f, T and N) are fixed, and Newton's method is used to find the maximum growth rate γ as a function of the tangent of the propagation angle α for each choice of $(\bar{\Lambda}, \delta\Lambda)$.

Figure 3 presents a stability-regime diagram in $(\bar{\Lambda}, \delta\Lambda)$-space, showing slope α^{-1} (shading) and growth rate γ (contours) for the fastest-growing inviscid unstable mode when $f = 1.5\times10^{-6}\,\mathrm{s}^{-1}$ (representing a small near-equatorial value), $T = 22$ days, and $N = 0.015\,\mathrm{s}^{-1}$. The algorithm outlined in the previous paragraph is unreliable for very small $\delta\Lambda$ and the range of $\delta\Lambda$ is therefore limited from below by $0.1 \times 10^{-6}\,\mathrm{s}^{-1}$ in figure 3. The bottom right-hand region of the diagram is dominated by II, for which γ increases rapidly with increasing $\bar{\Lambda}$ above the critical value f and the dominant disturbances are horizontal (i.e. $\alpha^{-1} = \infty$). Oscillatory shear ($\delta\Lambda \neq 0$) tends to reduce the growth rates associated with II, and the width of the II region shrinks as $\delta\Lambda$ increases. Immediately to the left of the II-dominated region there are PSI-type instabilities. There is a dramatic change in the dominant α^{-1} (from infinity to finite values) across the boundary separating the II-dominated and PSI-dominated regimes. Note that the dominant growth rates associated with PSI are independent of $\bar{\Lambda}$ for a wide range of $\bar{\Lambda}$ and increase linearly with $\delta\Lambda$. For $\delta\Lambda \to 0$, the dominant α can alternatively be found from the dominant resonance condition

$$\frac{\pi}{T} = \sqrt{f(f - \bar{\Lambda}) + N^2\alpha^2}, \tag{3.23}$$

which yields

$$\alpha^2_{dom}|_{\delta\Lambda\to 0} = \frac{\pi^2}{T^2N^2} - \frac{f(f - \bar{\Lambda})}{N^2}. \tag{3.24}$$

The dominant α^{-1} therefore increases with decreasing $\bar{\Lambda}$. At $\bar{\Lambda}_c = f - \pi^2/fT^2 \approx -3.2\times10^{-7}\,\mathrm{s}^{-1}$, the dominant α^{-1} becomes infinite. Further to the left, the right-hand side of (3.24) becomes negative and there are no values of α that can satisfy the dominant resonance condition (3.23). This induces the growth rate curves to turn upwards.

When vertical mixing is included, the growth rate is no longer merely a function of α for a fixed set of environmental parameters, as it also now depends on the magnitude of the vertical wavenumber m. To compare with the remaining solutions presented later, we present the results for a finite-size vertically periodic domain of height $H = 200\,\mathrm{m}$ and meridional half-width $L = 100\,\mathrm{km}$.

Figure 4 shows the vertical modenumber, $m^* = mH/2\pi$, and growth rate γ for the fastest-growing instability when $\ell = \pi/(2L)$, for $\nu = 10^{-6}\,\mathrm{m}^2\,\mathrm{s}^{-1}$. Because the dominant vertical mode is now a discrete variable, the dominant growth rates are no longer independent of $\bar{\Lambda}$. This accounts for the wavy (rather than flat, as in figure 3) appearance of the growth rate curves in figure 4. High-order vertical modes dominate the II-dominated region (bottom right-hand corner), but with finite values of m^* that decrease with $\bar{\Lambda}$ because of the viscosity; in addition, the critical value of $\bar{\Lambda}$ for II instability is now somewhat larger than f. In the rest of the parameter space, lower vertical modes dominate the flow. The analysis shows that these modes are excited via the PSI mechanism and anomalous Q plays no role in destabilizing them.

To obtain solutions to other forms of $\Lambda(t)$, we solve (3.2) numerically. The square-wave analytic solution turns out to be a good approximation to other forms of periodic time dependence. Figure 5 compares the inviscid stability diagram in the $(\bar{\Lambda}, \delta\Lambda)$-parameter space for square-wave time dependence to that of a cosine-wave time dependence. To capture both types of instability in the same graph, we plot the growth rate for vertical mode $m^* = 14$ ($m = 0.44\ \mathrm{m}^{-1}$), which experiences both II (the region in the lower right-hand corner) and PSI (everywhere else). The general properties of the two diagrams are very similar.

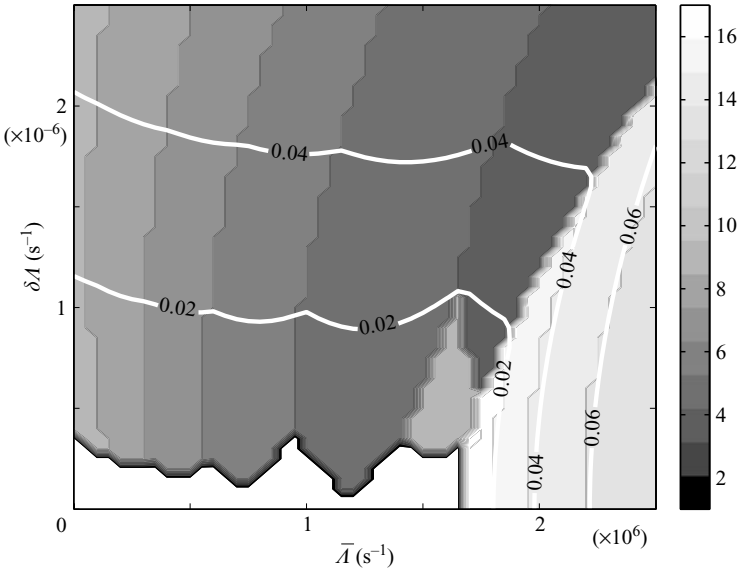

FIGURE 4. A stability-regime diagram in $(\bar{\Lambda}, \delta\Lambda)$-space and on the f-plane, plotting vertical mode number m^* (shading) and growth rate γ in days $^{-1}$ (contours) for the fastest-growing unstable mode, when the environmental parameters have the values given in the text and $\nu = 10^{-6}\,\mathrm{m^2\,s^{-1}}$.

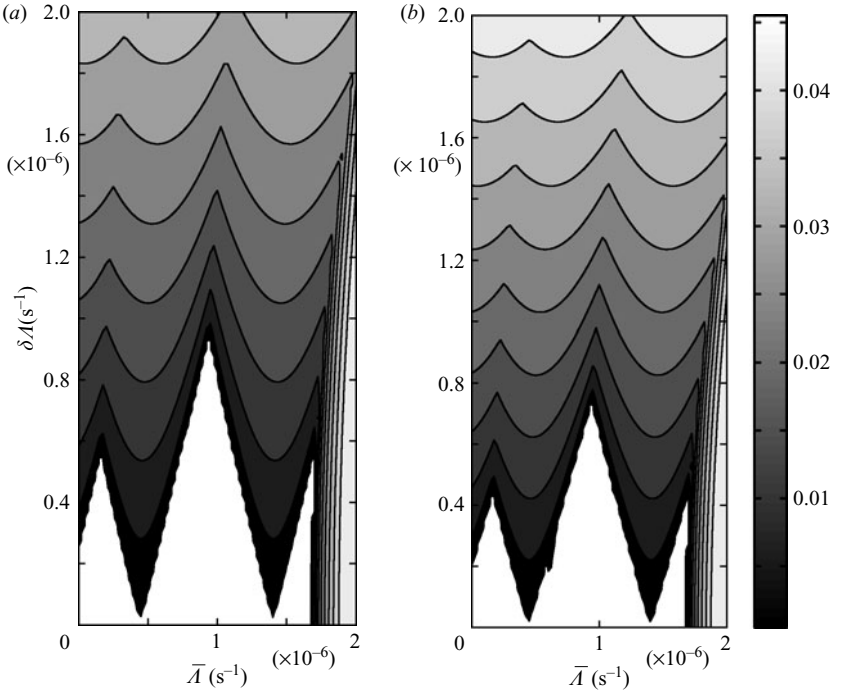

FIGURE 5. Stability-regime diagrams in $(\bar{\Lambda}, \delta\Lambda)$-space and on the f-plane, plotting growth rate γ (days^{-1}) for the fastest-growing inviscid unstable modes when $m^* = 14$ and the environmental parameters have the values given in the text. Solutions are shown for background flows with (*a*) square-wave and (*b*) sinusoidal time dependence.

3.2. *Equatorial β-plane solutions*

A more geophysically relevant situation arises in the equatorial ocean and atmosphere, where traditional II occurs whenever the background flow has a non-zero meridional shear at the equator. There is also strong time dependence due to large-scale equatorial free waves, allowing the possibility of PSI. The question then arises as to which of the two instabilities plays a more important role and how they interact. In considering the equatorial case in this section, we extend the results of d'Orgeville & Hua (2005) to the case when both steady and oscillatory meridional shear are present in the system.

On the equatorial β-plane, solutions to (2.4) can be represented as the expansions

$$v_m(y,t) = \sum_{j=0}^{\infty} v_{mj}(t)\,\phi_j(\eta_m), \tag{3.25}$$

where the ϕ_j are Hermite functions defined by

$$\phi_j(\xi) = \frac{(-1)^j}{(2^j\, j!\sqrt{\pi})^{1/2}} \exp\left(\tfrac{1}{2}\xi^2\right) \frac{\mathrm{d}^j}{\mathrm{d}\xi^j} \exp(-\xi^2), \tag{3.26}$$

with

$$\eta_m = \sqrt{\frac{\beta|m|}{N}}\left(y - y'\right) \tag{3.27}$$

and y' is an arbitrary constant.

3.2.1. *Inertial instability*

As for the f-plane case, we review properties of inertial instability for steady background flow when $\Lambda(t) = \bar{\Lambda}$. Setting

$$y' = \frac{\bar{\Lambda}}{2\beta} \tag{3.28}$$

in (3.27), we find that v_{mj} satisfies (3.2) with

$$\sigma_{mj}^2 = (2j+1)\frac{\beta N}{m} - \frac{\bar{\Lambda}^2}{4}. \tag{3.29}$$

Solutions have the form (3.4) with $s^{\pm}$ given by (3.5). The latitude y' defined by (3.28) coincides with the centre of the anomalous Q region and is called the *dynamic equator*. Instability occurs when

$$\bar{\Lambda}^2 > \frac{4\beta N}{|m|} + 4\nu^2 m^4 \tag{3.30}$$

(Dunkerton 1981). Note that, in contrast to the f-plane case, inviscid unstable solutions always exist for any non-zero $\bar{\Lambda}$.

According to (3.29), there is a low vertical wavenumber cutoff for unstable modes (Griffiths 2003*a*),

$$|m| > \frac{4\beta N}{\bar{\Lambda}^2}. \tag{3.31}$$

The most unstable mode has a vertical wavelength determined by ν, and its meridional structure is the $j = 0$ Hermite function (a Gaussian) centred on the dynamic equator. The characteristic meridional scale of the perturbation is given by the Rossby radius of deformation $N/(\beta|m|)$ and is therefore proportional to its vertical scale. For values of y' sufficiently larger than the Rossby radius of deformation for a given unstable

mode, we expect that such a mode would experience f-plane-like linear dynamics with f set to $\beta y'$.

3.2.2. *Time-dependent instability*

For the analysis of time-dependent instability, it is convenient to non-dimensionalize the governing equations. We use the same scaling as d'Orgeville & Hua (2005)

$$\{t, T, \Lambda^{-1}\} = \sqrt{\frac{|m|}{\beta N}}\,\{t^*, T^*, \Lambda^{*,-1}\}, \qquad y = \sqrt{\frac{N}{\beta|m|}}\,y^*, \tag{3.32}$$

where t^*, T^*, Λ^* and y^* are non-dimensionalized time, background flow oscillation period, background shear, and latitude, respectively.

With the asterisks and index m dropped, (2.4) becomes

$$\left(\mathscr{D}^2 - \partial_{yy} + y^2 - y\bar{\Lambda} - y\delta\Lambda\cos\frac{2\pi t}{T}\right) v = 0, \tag{3.33}$$

where we now set $\Lambda(t)$ to the form of a cosine wave (equation (3.8)). Transforming the meridional coordinate to

$$\eta = y - \tfrac{1}{2}\bar{\Lambda}, \tag{3.34}$$

we obtain

$$\left(\mathscr{D}^2 - \partial_{\eta\eta} + \eta^2 - \frac{\bar{\Lambda}^2}{4} - \delta\Lambda\left(\eta + \frac{\bar{\Lambda}}{2}\right)\cos\frac{2\pi t}{T}\right) v = 0. \tag{3.35}$$

Substituting the Hermite function expansion (3.25) into (3.35), and using the defining equation

$$\frac{\partial^2\phi_j}{\partial\eta^2} - \eta^2\phi_j = -(2j+1)\phi_j, \tag{3.36}$$

yields

$$\sum_{j=0}^{\infty}\left[\phi_j\mathscr{D}^2 v_j + (2j+1)v_j\phi_j - \frac{\bar{\Lambda}^2}{4}v_j\phi_j\delta\Lambda\left(\eta + \frac{\Lambda}{2}\right)\cos\left(\frac{2\pi t}{T}\right)v_j\phi_j\right] = 0. \tag{3.37}$$

Finally, using the identity

$$\eta\phi_j = j\phi_{j-1} + \tfrac{1}{2}(\phi_{j+1}), \tag{3.38}$$

we can eliminate the products $\eta\phi_j$ to obtain

$$\mathscr{D}^2 v_j + \left(2j + 1 - \frac{\bar{\Lambda}^2}{4}\right)v_j - \delta\Lambda\cos\left[\frac{2\pi t}{T}\right]\left\{\frac{1}{2}v_{j-1} + \frac{\bar{\Lambda}}{2}v_j + (j+1)v_{j+1}\right\} = 0. \tag{3.39}$$

The system studied in d'Orgeville & Hua (2005) is a special case of (3.39) obtained by setting $\bar{\Lambda} = 0$.

In contrast to the f-plane case, the equatorial β-plane dynamics linearized around an oscillating background flow is governed by an infinite set of coupled ordinary differential equations. We find, however, that solutions were well converged when the set was truncated at $j = 10$. To determine the solution of the system, we resort to numerical Floquet analysis: we integrate the truncated system (3.39) in time for one period T using a fourth-order Runge–Kutta algorithm and calculate the eigenvalues of the resulting Floquet matrix using a MATLAB eigensolver. We also obtained solutions to (3.35) using a second-order finite-difference spatial discretization in y instead of a Hermite expansion, verifying our results.

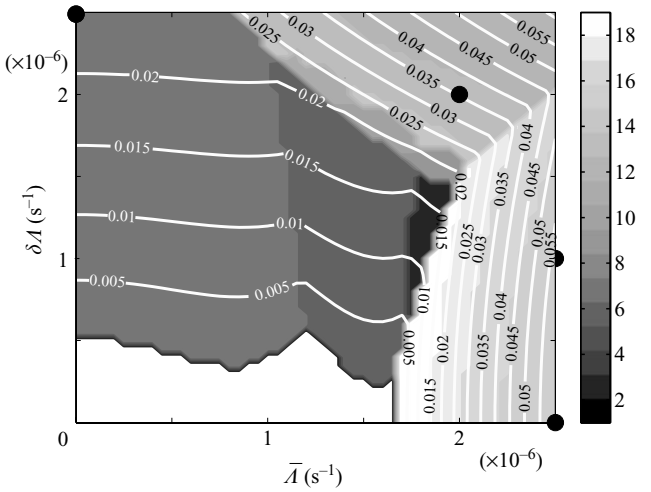

FIGURE 6. A stability-regime diagram in $(\bar{\Lambda}, \delta\Lambda)$-space and on the equatorial β-plane, plotting vertical mode number m^* (shading) and growth rate γ in days^{-1} (contours) for the fastest growing, unstable mode, when the environmental parameters have the values listed in the text and $\nu = 10^{-6}\,\mathrm{m^2\,s^{-1}}$ and for a background flow with time dependence. The circles mark the parameter regimes of nonlinear solutions discussed in § 4.

The solutions are presented in dimensional form. Figure 6 presents a stability-regime diagram in $(\bar{\Lambda}, \delta\Lambda)$-space, plotting m^* and γ for the fastest-growing instability when $\nu = 10^{-6}\,\mathrm{m^2\,s^{-1}}$, $\beta = 2.29 \times 10^{-11}\,\mathrm{m^{-1}\,s^{-1}}$, and other parameter values are the same as for the f-plane case (except for L, which is effectively infinite in our linear model). As in the f-plane case, there is a sharp boundary between the regions of II and PSI dominance at low $\delta\Lambda$ and a sharp disparity in dominant wavenumbers across that boundary. For the chosen parameters, the critical value of steady shear is $\bar{\Lambda} \approx 1.67 \times 10^{-6}\,\mathrm{s^{-1}}$ (Griffiths 2003*a*), and the dominant vertical mode at the critical shear is $m^* = 19$, corresponding to vertical wavenumber $m \approx 0.6\,\mathrm{m^{-1}}$. In contrast, there is a new 'wedge region' in the upper-right-hand corner, where, even though the dominant instability mechanism is PSI, the gravest modes have high vertical modenumber, similar to II-favoured modes. Their meridional structure, however, is different from the II-favoured Gaussian, which are centred on the dynamic equator; instead, it resembles an order-one Hermite function with a zero crossing between the two dynamic equators representative of the background shears $\bar{\Lambda} + \delta\Lambda$ and $\bar{\Lambda} - \delta\Lambda$. The wedge-region modes are also similar to the II modes in that they are highly sensitive to ν. Indeed, there is no viscosity-independent vertical-scale selection in this regime, indicating that the selection must be determined by nonlinear processes.

4. Nonlinear solutions

In this section, we investigate the finite-amplitude stage in the development of near-equatorial perturbations, finding solutions to the nonlinear model (2.3) on the equatorial β-plane. Values for model parameters are given in table 1; they are essentially the same as those used for the linear equatorial β-plane solutions, except for the inclusion meridional viscosity ν_h and diffusivity κ_h required for numerical stability.

Parameter	Value	Interpretation
β	2.29×10^{-11} m^{-1}s^{-1}	Gradient of Coriolis parameter
g	9.78 m s^{-2}	Acceleration due to gravity
ρ_*	1020 kg m^{-3}	Reference density
T	22 days	Forcing period
H	200 m	Domain height
L	500 km	Domain half-width
N	0.015 s^{-1}	Background buoyancy frequency
ν_h	50 m^2 s^{-1}	Horizontal viscosity
ν_v	10^{-6} m^2 s^{-1}	Vertical viscosity
κ_h	50 m^2 s^{-1}	Horizontal diffusivity
κ_v	10^{-6} m^2 s^{-1}	Vertical diffusivity

TABLE 1. Default parameters for the nonlinear model.

Run	$\bar{\Lambda}$	$\delta\Lambda$
II	2.5	0
II+	2.5	1.0
PSI	0	2.5
MI	2.0	2.0

TABLE 2. Initial time-mean shear $\bar{\Lambda}$ and oscillating shear magnitude $\delta\Lambda$ in 10^{-6} s^{-1} for experiments described in § 4.

The initial background zonal velocity profile is set at $U(t=0, y) = \left(\bar{\Lambda} + \delta\Lambda\right)$. An initial perturbation is introduced to (2.3) by adding

$$\delta\rho(y, z) = \epsilon \cos\left(\frac{\pi y}{Y}\right) \sum_{m^*=1}^{20} \cos\left(\frac{2\pi m^* z}{H} + \varphi_{m^*}\right) \tag{4.1}$$

to ρ_b in the strip $-Y < y < Y$, where $\epsilon = 5 \times 10^{-2}$ kg m^{-3}, $Y = 160$ km, and phases φ_{m^*} are random numbers between $-\pi$ and π. We found that a grid resolution of $\Delta y = 6.1$ km and $\Delta z = 2$ m provides sufficient resolution for most experiments; when it did not, the resolution was doubled both horizontally and vertically. A time step of 30 s is sufficient to ensure numerical stability throughout the evolution.

In order to identify the presence of interleaving structures, we also integrate an equation such as (2.3*c*) for a passive tracer S. The initial state of S is given by

$$S_b(y, z) = S_0 + S_y y, \tag{4.2}$$

where $S_y = -5 \times 10^{-6}$ psu m^{-1}, a simple representation of the observed salinity field in the near-equatorial thermocline of the equatorial Pacific.

In the following, we describe four experiments designed to investigate nonlinear development of the instabilities found in the previous section. The parameter regimes in these experiments qualitatively correspond to the cases of pure II (run II), influence of oscillatory shear on II (run II+), pure PSI (run PSI) and mixed instabilities (run MI). The background flow for each experiment is specified in table 2, and marked by dots on the β-plane stability regime diagram in figure 6.

4.1. *Pure II*

The nonlinear equilibration of inertially unstable steady jets has been studied by Hua *et al.* (1997) and by Griffiths (2003*a*, *b*). They found that as the perturbation reaches substantial amplitude, a region of anomalously low potential vorticity of the vertically averaged state $q = f - (1/H)\int_0^H u_y \, dz$ forms and then spreads poleward as the magnitude of q decreases. In the final state, fq approaches 0 in the region affected by II. When there is a forcing that maintains the background current, the system reaches a steady state with an equilibrated finite-amplitude disturbance. In its absence, Griffiths (2003*a*) found that the disturbance eventually decays, leaving behind a modified vertically independent background state with nearly zero potential vorticity in the initially unstable region.

Here, we consider an unstable case with $\bar{\Lambda} = 2.5 \times 10^{-6}$ s^{-1} and $\delta\Lambda = 0$, for which the region of anomalous Q is between the equator and 90 km north of the equator. Snapshots of fields filtered for each vertical mode separately (not shown) indicate that the spatial structure of the disturbances is initially the same as predicted from linear instability theory: the meridional velocity v is represented by a Gaussian centred on the dynamic equator approximately 45 km north of the equator, the perturbation zonal velocity u is phase-locked to, and is negatively correlated with, v in the unstable region, and the growth rate is approximately 0.06 days^{-1}. For comparison with earlier studies, it is useful to characterize the strength of the II in terms of a non-dimensional growth rate $\hat{s} = s/(\bar{\Lambda}/2)$. Our parameters correspond to $\hat{s} = 0.57$, about midway between the weakly unstable regime $0 < \hat{s} \leqslant 0.25$ of Griffiths (2003*a*) and the strongly unstable regime of Griffiths (2003*b*) ($0.75 < \hat{s} \leqslant 0.88$).

Because u and v are negatively correlated as the perturbation grows, the meridional advection of perturbation zonal velocity is such that cells with eastward perturbation zonal velocity are advected towards the equator and cells with westward perturbation zonal velocity are advected poleward. In terms of the spectrum of vertical modes, this rearrangement appears as a cascade into higher and lower vertical modes. Figure 7(*a*) shows the vertical-mode (m^*) spectrum of the kinetic energy as a function of time. At day 110, the energy is distributed over a broadband of vertical modes. At later times, the band narrows to a few vertical modes with a vertical modenumber $m^* = mH/(2\pi) = 10$. This value falls between the gravest linear mode $m^* = 13$ and the buoyancy cutoff mode $m^* = 7$, which is indicative of a slight upscaling. This is similar to the least unstable simulation of Griffiths (2003*b*) (his figures 3 and 4).

Density overturns first begin to appear at the poleward boundary of the anomalous-Q region. The maximum of the perturbation streamfunction moves towards the equator, but the perturbation density stays asymmetric. For the vertically averaged flow, this implies that corrections to the zonal flow are eastward near the equator and westward away from the equator. As a result, meridional shear in the initially unstable region is decreased and the flow becomes less unstable. The adjusted q and fq tend to be homogenized, thus eliminating the unstable region (figures 7*b*, *c*). Griffiths (2003*a*) has shown that further development is determined by whether the vertically averaged flow becomes completely stabilized before the unstable modes reach overturning amplitudes (as in weakly unstable cases) or after (as in the case reported here). In the latter case, the disturbance grows to a large amplitude and overturning becomes an important part of the neutralization process.

Griffiths (2003*b*) argues that in a strongly unstable case, the vertical scale that is eventually selected is approximately the low-cutoff wavenumber for II, i.e. $m \approx 4\beta N/\bar{\Lambda}^2 = 0.22\,\mathrm{m}^{-1}$, which roughly corresponds to a vertical scale of 30 m. In our case, the selected vertical scale is much smaller. Figure 7(*d*) shows the tracer field

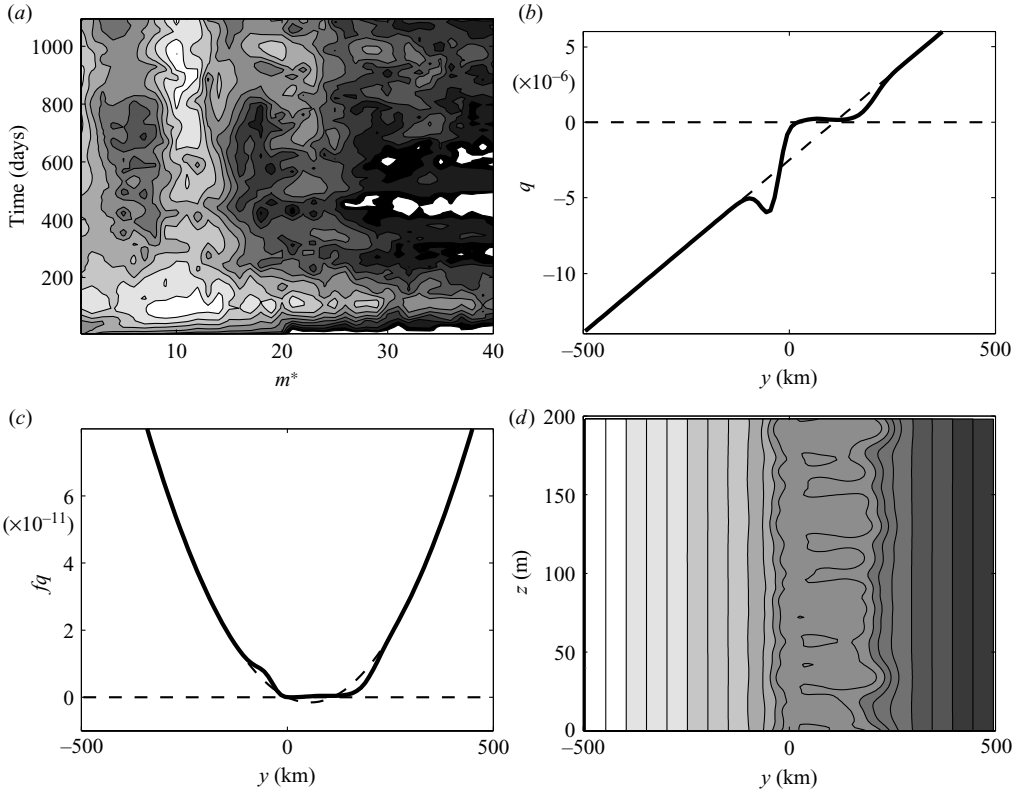

FIGURE 7. Plots illustrating the response of the nonlinear model for a background current dominated by II, showing (*a*) the time evolution of the vertical-mode (m^*) spectrum of the kinetic energy, and snapshots of (*b*) q, (*c*) fq, and (*d*) the tracer field S at day 165. m^*-spectrum of the kinetic energy is defined as $(1/2)\rho_0 \sum_{l^*}(|\hat{u}(l^*, m^*, t)|^2 + |\hat{v}(l^*, m^*, t)|^2)$, where $\hat{u}(l^*, m^*, t)$ and $\hat{v}(l^*, m^*, t)$ are Fourier transforms of the velocity fields $u(y, z, t)$ and $v(y, z, t)$, respectively.

at the time of maximum disturbance amplitude (day 165), and the intrusions have vertical scales between 10 and 20 m. However, it is still reasonable to characterize the II in the case described here as strong, because the intrusions have a meridional extent over 200 km – more than twice exceeding the confines of the initially unstable region. For comparison, in the weakly nonlinear cases of Griffiths (2003*a*), the disturbances extend poleward to at most about 3/2 the width of the unstable region.

4.2. *Effect of oscillatory shear on II*

As expected from the linear theory developed in § 3, oscillatory shear tends to suppress inertial instability and enhance the growth of the PSI-favoured modes. When a small oscillatory shear ($\delta\Lambda \leqslant 0.7 \times 10^{-6}\ \mathrm{s}^{-1}$) is added to a strongly inertially unstable initial time-mean shear, its effects are small and the inertial instability proceeds in a similar manner as before. With a somewhat larger $\delta\Lambda$ ($\geqslant 0.7 \times 10^{-6}\ \mathrm{s}^{-1}$), there are significant changes to the time development of the flow (figure 8*a*). Initially, the II mode proceeds in a similar manner as in the case of a steady shear, although the amplitude is weakened. At later times, however, the PSI-favoured vertical modes 3, 5 and 7 come into prominence. Because the meridional structure of these modes is represented by higher-order Hermite functions, this result is sensitive to meridional viscosity. For a meridional viscosity ten times the default value, PSI favours vertical modes 3 and

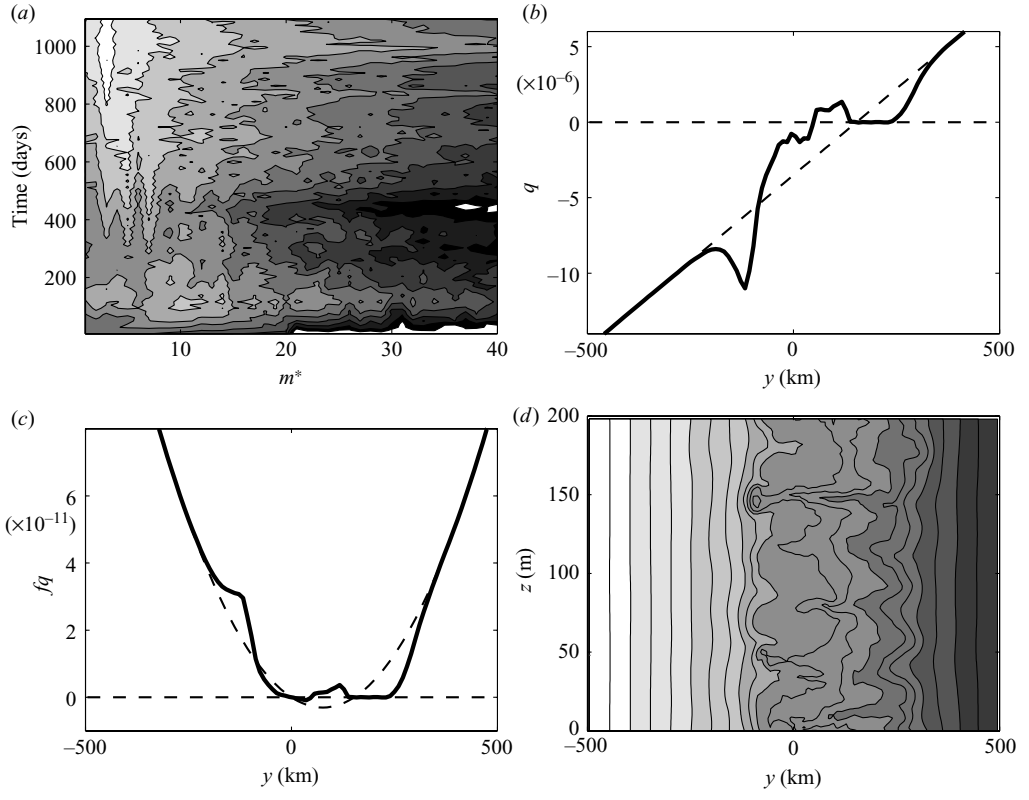

FIGURE 8. As in figure 7, except for solution II+ with the snapshots at day 1078.

5 instead of 5 and 7. Note that although II has the fastest linear growth rate, it is PSI that dominates the later stages of development: because of the lower vertical wavenumber associated with the PSI modes, they can reach higher amplitudes without overturning.

The modifications to the background flow are such that q and fq are partially mixed. Figures 8(b) and 8(c) show the adjusted q and fq when the phase of the background oscillatory flow is zero (corresponding to the moment of time when the overall background shear is at its maximum, i.e. $\bar{\Lambda} + \delta\Lambda$). The extent of the mixed region is determined by the amplitude of the dominant disturbance and extends to the north substantially further than in the steady case. South of the equator, the nonlinear development of the instability creates a region of strong curvature in the zonal velocity profile, which may come to play an important role in a fully three-dimensional flow where barotropic and baroclinic instabilities are possible (Limpasuvan *et al.* 2000). Although steady-state II also tends to create regions of strong curvature, their magnitude is considerably weaker (compare figures 7b and 8b).

A snapshot of the tracer field at day 1078 is shown in figure 8(d). Intrusions extend about 300 km north of the equator; well beyond the northernmost boundary of the anomalous Q region ($\sim$130 km). The intrusions also extend farther south than in the steady-state case, some reaching -100 km. The vertical scale of the intrusions is much less well-defined than in the steady case. There has been substantial lateral mixing of the tracer between $y = -100$ and 200 km.

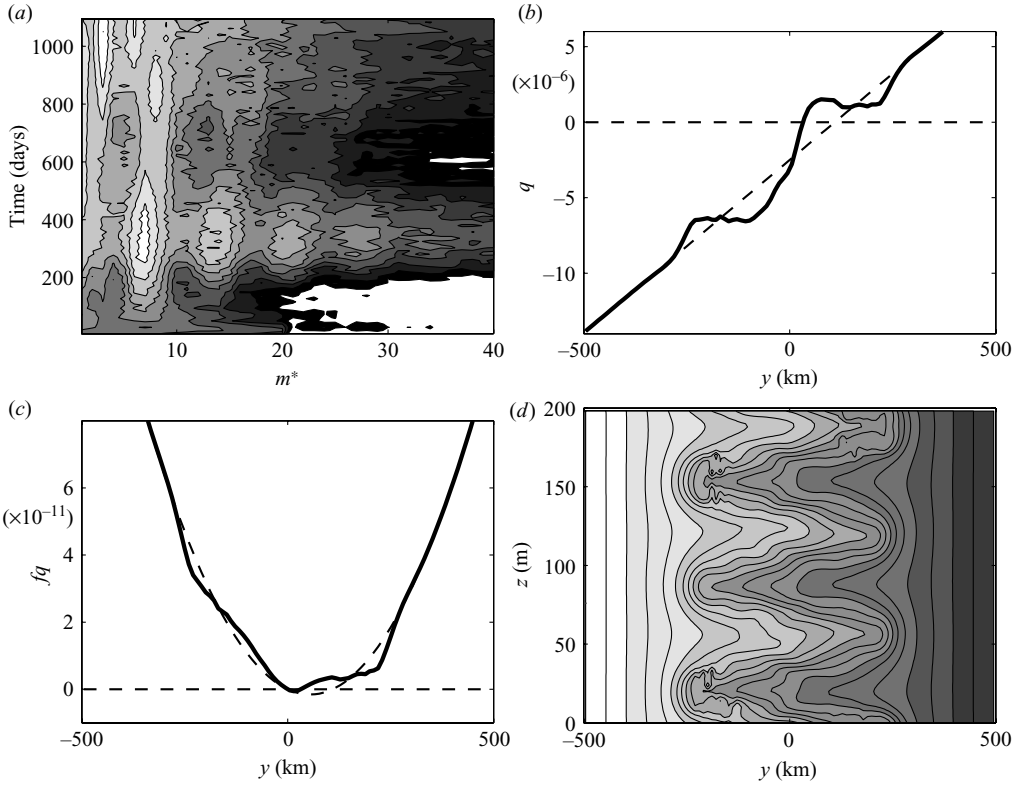

FIGURE 9. As in figure 7, except for solution PSI with the snapshots at day 1078.

4.3. *Pure PSI*

At the opposite extreme in our study is the case when the background shear is purely oscillatory ($\bar{\Lambda} = 0$). Figure 9 illustrates the solution when $\bar{\Lambda} = 0$ and $\delta\Lambda = 2.5 \times 10^{-6}\,\mathrm{s}^{-1}$. Experiments with values of $\delta\Lambda$ between $1.5 \times 10^{-6}\,\mathrm{s}^{-1}$ and $2.8 \times 10^{-6}\,\mathrm{s}^{-1}$ produce qualitatively similar results (with, respectively, slower/higher growth rates during the initial growth stage), while for $\delta\Lambda$ less than $1.5 \times 10^{-6}\,\mathrm{s}^{-1}$, the background flow is stabilized before any overturning occurs. We did not attempt any simulations with $\delta\Lambda$ larger than $2.8 \times 10^{-6}\,\mathrm{s}^{-1}$.

In accordance with the linear theory of § 3.2, the initial phase is dominated by the growth of the vertical mode $m^* = 7$ (figure 9*a*). In contrast to the pure II case, other vertical modes initially do not experience substantial growth and the spectrum remains nearly monochromatic throughout the initial phase. The meridional structure of the gravest disturbance projects mostly onto the zeroth and first Hermite functions centred on the equator, and is not sensitive to meridional viscosity.

By day 300, there is a cascade of energy into the higher harmonics of the dominant mode 7. All harmonics reach their peak amplitude at approximately the same time. At that time, the Richardson number associated with the meridional velocity field decreases to its critical value of 1/4 in some locations, leading to overturning, which subsequently weakens all the vertical modes with viscosity eliminating the highest modes most rapidly. The highest vertical mode shown (mode 35) is the first to dissipate, followed at later times by modes 28, 21 and 14. Mode $m^* = 7$ loses some energy, but remains strong for some time after its higher harmonics have dissipated.

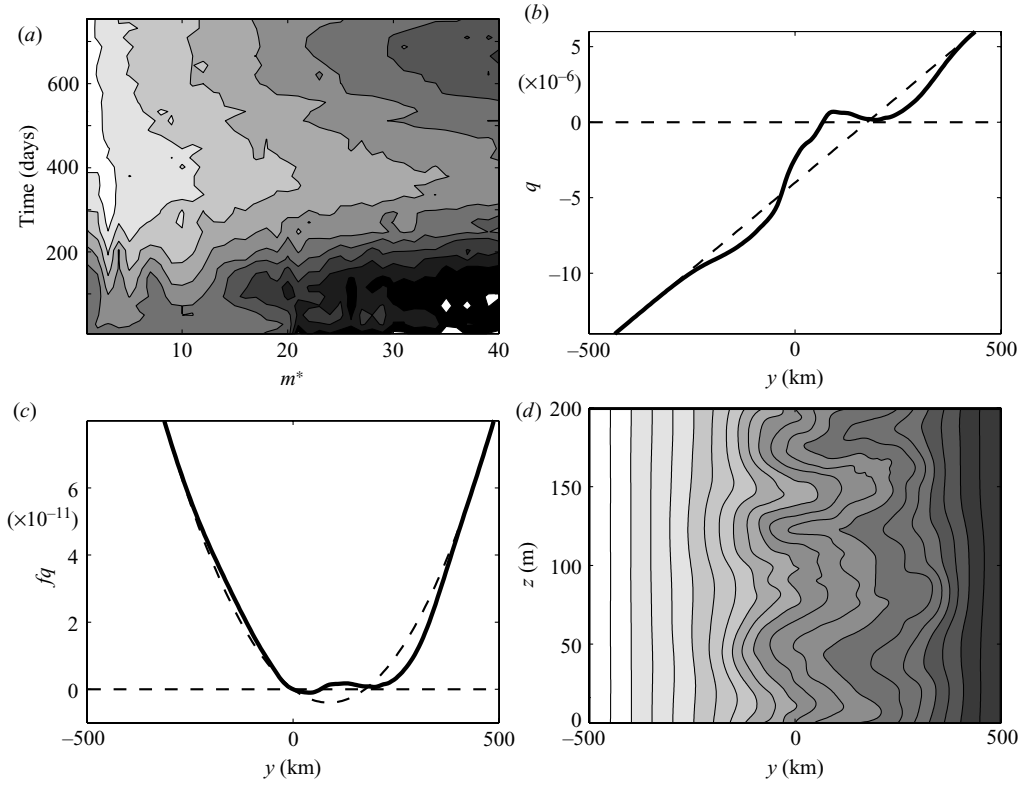

FIGURE 10. As in figure 7, except for solution MI with the snapshots at day 880.

As the vertically averaged state is modified, the modes that were originally unstable begin to oscillate faster and are no longer capable of extracting energy from the background flow. A linear stability analysis of this modified state shows that a higher vertical mode now oscillates at an appropriate frequency and experiences growth through PSI. Figure 9(*a*) shows that after the overturning event, the dominant mode shifts to $m^* = 8$, and the $m^* = 3$ mode dominates even later, at a time when the disturbance reaches its largest amplitude. The figure is terminated at a finite time, but the $m^* = 3$ mode continues to dominate the evolution for yet longer time.

Figures 9(*b*) and 9(*c*) show the snapshots of q and fq at day 1078, when the phase of the background shear is at its maximum. Unlike the II scenario, the vertically averaged q is not homogenized near the equator. In the immediate vicinity of the equator the vertically averaged shear, in fact, becomes much more positive than the initial shear, but the vertically averaged flow remains inertially stable, since fq is still positive. Now the adjusted mean q is relatively uniform in two regions approximately 100 km wide north and south of the equator. A snapshot of the tracer field on day 1078 shows the dominance of vertical mode 3 (figure 9*d*), and the intrusions extend from about −250 km to +250 km.

4.4. *Mixed instabilities*

With $\bar{\Lambda} = \delta\Lambda = 2 \times 10^{-6}\,\mathrm{s}^{-1}$, the system lies in the wedge (mixed-instability) region in the upper-right-hand corner of the linear stability diagram (figure 6). Figure 10(*a*) shows the evolution of the vertical mode spectrum of the kinetic energy for this case. Initially, significant kinetic energy appears in modes 3, 5 and 10, leading to a broadband vertical mode spectrum, once the disturbances reach large amplitude, that

is quite different from the pure PSI and pure II cases. At later times, the spectrum decreases monotonically with m^*. Figures 10(*b*) and 10(*c*) show snapshots of q and fq at day 880, when the phase of the background shear is at its maximum. Overall, the curves are similar to their counterparts for the pure II case (figures 7*b* and 7*c*) except with a much broader meridional extent. The region of anomalous q is almost eliminated, and q is homogenized over a large meridional extent north of the equator where its value is almost zero. The zonal flow curvature to the south of the equator is much weaker than in the II+ case and is qualitatively similar to the pure II scenario. A snapshot of the tracer field (figure 10*d*) shows the presence of a wide range of vertical scales, in contrast to pure II and similar to the late stages of the II+ case, and the intrusions extend from about −100 km to +350 km.

5. Summary and discussion

We have shown that time-dependence can dramatically modify the stability characteristics of zonal currents in the ocean. With time dependence, instability can be manifested as a traditional inertial instability (II), a parametric subharmonic type (PSI), and a mixture of both types. We investigate a two-parameter family of time-dependent background flows, the parameters being the magnitudes of the background time-mean $\bar{\Lambda}$ and oscillatory $\delta\Lambda$ shears, and we provide a quantitative description of the instability regimes in different parts of the parameter space.

A linear stability analysis on the f-plane shows that there is a clear separation between II-dominated and PSI-dominated regions in parameter space. II dominates for high $\bar{\Lambda}$ and low $\delta\Lambda$. If $\bar{\Lambda}$ is kept fixed at a value at which it is unstable for small $\delta\Lambda$, its growth rate decreases as $\delta\Lambda$ increases until a critical value is reached when the instability switches to PSI. PSI dominates when both $\bar{\Lambda}$ and $\delta\Lambda$ are high. Consideration of the same type of background flows on the equatorial β-plane gives similar results, with PSI and II being well separated throughout most of the parameter space. In addition, there is a distinct region for high values of $\bar{\Lambda}$ and $\delta\Lambda$ where there is an interaction between the two instability mechanisms (mixed instability).

For steady background shear, the nonlinear time-development proceeds by the route described in Griffiths (2003*a*) and Hua *et al.* (1997). When the background shear is time dependent, there are similarities to the steady-shear case, but important differences as well, particularly concerning the meridional extent of intrusions. When II is not too strong, II-favoured modes equilibrate at low amplitude because of their high vertical wavenumber (either through vertical viscosity or overturning) and do not produce tracer interleaving patterns of large meridional extent. In contrast, PSI-favoured modes, even though they have a slower growth rate, usually grow to a higher amplitude, producing interleaving patterns with a meridional scale of the order of 300 km.

Such interleavings are likely to be an important mixing process in the equatorial ocean (note the evidence of lateral mixing shown for cases II, II+ and MI in figures 7*d*, 8*d*, and 10*d*). On the basin scale, a nonlinear interplay between vertical and lateral mixing, leading to either direct damping of the internal dynamics by lateral dissipation (when the lateral mixing coefficient is large), or inducing accumulation of high vertical wavenumber activity near the equator accompanied by spuriously high vertical dissipation (when the lateral mixing coefficient is low) is well-documented (Maes, Madec & Delecluse 1997). There is growing evidence that to capture realistic equatorial circulation, a numerical model has to have a spatially non-uniform lateral diffusion coefficient (Large *et al.* 2001; Pezzi & Richards 2003). This non-uniformity, however, cannot be introduced just to make observations fit simulation outputs. To supply

models with predictive power such a parameterization must have a well-understood physical process behind it. In this work, we have identified several such processes and quantified their relative importance for different environmental parameter settings.

A limitation of this study is that the nonlinear model is forced in a simple way in order to maintain the background current. In the real equatorial ocean, the background current is also forced but in another way, by the adjustment to forcing by the large-scale wind field through the radiation of equatorially trapped waves. How do our results change when the background flow is forced more realistically, for example, by a mixed Rossby–gravity (Yanai) wave? Other limitations are the restrictions to one-dimensional background flows $U(y)$ and two-dimensional (y, z) instabilities. What is the impact when these restrictions are relaxed? We are currently extending our work to address these, and other, issues.

This work was supported by the NSF under grant OCE 03-26630. This paper is the School of Ocean Engineering Science and Technology Contribution Number SOEST no. 7156 and International Pacific Research Center Contribution Number IPRC-468. We would like to thank Bach Lien Hua for providing the numerical code for the nonlinear model and two anonymous referees for very helpful comments.

REFERENCES

Bender, C. M. & Orszag, S. A. 1978 *Advanced Mathematical Methods for Scientists and Engineers*. McGraw-Hill.

Dunkerton, T. J. 1981 On the inertial stability of the equatorial middle atmosphere. *J. Atmos. Sci.* **38**, 2354–2364.

Edwards, N. R. & Richards, K. J. 1999 Linear double-diffusive-inertial instability at the equator. *J. Fluid Mech.* **395**, 295–319.

Griffiths, S. D. 2003*a* The nonlinear evolution of zonally symmetric equatorial inertial instability. *J. Fluid Mech.* **474**, 245–273.

Griffiths, S. D. 2003*b* Nonlinear vertical scale selection in equatorial inertial instability. *J. Atmos. Sci.* **60**, 977–990.

Hua, B. L., Moore, D. W. & Le Gentil, S. 1997 Inertial nonlinear equilibration of equatorial flows. *J. Fluid Mech.* **331**, 345–371.

Large, W. G., Danabasoglu, G., McWilliams, J. C., Gent, P. R. & Bryan, F. O. 2001 Equatorial circulation of a global ocean climate model with anisotropic horizontal viscosity. *J. Phys. Oceanogr.* **31**, 518–536.

Lee, H. & Richards, K. J. 2004 The three-dimensional structure of the interleaving layers in the western equatorial pacific ocean. *Geophys. Res. Lett.* **31**, L07301, doi:10.1029/2004GL019441.

Limpasuvan, V., Leovy, C. B., Orsolini, Y. J. & Boville, B. A. 2000 A numerical simulation of the two-day wave near the stratopause. *J. Atmos. Sci.* **57**, 1702–1717.

Maes, C., Madec, G. & Delecluse, P. 1997 Sensitivity of an equatorial pacific ogcm to the lateral diffusion. *Mon. Weather Rev.* **125**, 958–971.

d'Orgeville, M. & Hua, B. L. 2005 Equatorial inertial-parametric instability of zonally symmetric oscillating shear flows. *J. Fluid Mech.* **531**, 261–291.

Pezzi, L. & Richards, K. J. 2003 The effects of lateral mixing on the mean state and eddy activity of an equatorial ocean. *J. Geophys. Res.* **108**, 3371.

Philander, G. 1990 *El Niño, la Niña, and the Southern Oscillation*. Academic.

Richards, K. J. & Banks, H. 2002 Characteristics of interleaving in the western equatorial pacific. *J. Geophys. Res.* **107** (C12), 3231, doi:10.1029/2001JC000971.

Richards, K. J. & Edwards, N. R. 2003 Lateral mixing in the equatorial pacific: the importance of inertial instability. *Geophys. Res. Lett.* **30**, 1888, doi:10.1029/2003GL017768.

Stevens, D. 1983 On symmetric stability and instability of zonal mean flows near the equator. *J. Atmos. Sci.* **40**, 882–893.

Stoker, J. J. 1950 *Nonlinear Vibrations in Mechanical and Electrical Systems*. Interscience.